

TOI-677 b: A Warm Jupiter (P=11.2d) on an eccentric orbit transiting a late F-type star

ANDRÉS JORDÁN,^{1,2} RAFAEL BRAHM,^{3,4,2} NÉSTOR ESPINOZA,⁵ THOMAS HENNING,⁶ MATÍAS I. JONES,⁷
DIANA KOSSAKOWSKI,⁶ PAULA SARKIS,⁶ TRIFON TRIFONOV,⁶ FELIPE ROJAS,^{4,2} PASCAL TORRES,^{4,2} HOLGER DRASS,³
SANGEETHA NANDAKUMAR,⁸ MAURO BARBIERI,⁸ ALLEN DAVIS,⁹ SONGHU WANG,⁹ DANIEL BAYLISS,¹⁰ LUKE BOUMA,¹¹
DIANA DRAGOMIR,¹² JASON D. EASTMAN,¹³ TANSU DAYLAN,^{14,15} NATALIA GUERRERO,¹⁴ THOMAS BARCLAY,^{16,17}
ERIC B. TING,¹⁸ CHRISTOPHER E. HENZE,¹⁸ GEORGE RICKER,¹⁴ ROLAND VANDERSPEK,¹⁴ DAVID W. LATHAM,¹³
SARA SEAGER,^{14,19,20} JOSHUA WINN,¹¹ JON M. JENKINS,¹⁸ ROBERT A. WITTENMYER,²¹ BRENDAN P. BOWLER,²²
IAN CROSSFIELD,²³ JONATHAN HORNER,²¹ STEPHEN R. KANE,²⁴ JOHN F. KIELKOPF,²⁵ TIMOTHY D. MORTON,²⁶
PETER PLAVCHAN,²⁷ C.G. TINNEY,²⁸ BRETT ADDISON,²¹ MATTHEW W. MENGEL,²¹ JACK OKUMURA,²¹ SAHAR SHAHAF,²⁹
TSEVI MAZEH,²⁹ MARKUS RABUS,^{30,31} AVI SHPORER,¹⁴ CARL ZIEGLER,³² ANDREW W. MANN,³³ AND RHODES HART²¹

¹Facultad de Ingenieria y Ciencias, Universidad Adolfo Ibáñez, Av. Diagonal las Torres 2640, Peñalolén, Santiago, Chile

²Millennium Institute for Astrophysics, Chile

³Center of Astro-Engineering UC, Pontificia Universidad Católica de Chile, Av. Vicuña Mackenna 4860, 7820436 Macul, Santiago, Chile

⁴Instituto de Astrofísica, Pontificia Universidad Católica de Chile, Av. Vicuña Mackenna 4860, Macul, Santiago, Chile

⁵Space Telescope Science Institute, 3700 San Martin Drive, Baltimore, MD 21218, USA

⁶Max-Planck-Institut für Astronomie, Königstuhl 17, Heidelberg 69117, Germany

⁷European Southern Observatory, Alonso de Córdova 3107, Vitacura, Casilla 19001, Santiago, Chile

⁸INCT, Universidad de Atacama, calle Copayapu 485, Copiapó, Atacama, Chile

⁹Department of Astronomy, Yale University, New Haven, CT 06511, USA

¹⁰Department of Physics, University of Warwick, Coventry CV4 7AL, UK

¹¹Department of Astrophysical Sciences, Princeton University, 4 Ivy Lane, Princeton, NJ 08540, USA

¹²Department of Physics and Astronomy, University of New Mexico, 1919 Lomas Blvd NE, Albuquerque, NM 87131, USA

¹³Harvard-Smithsonian Center for Astrophysics, 60 Garden St, Cambridge, MA 02138, USA

¹⁴Department of Physics and Kavli Institute for Astrophysics and Space Research, Massachusetts Institute of Technology, Cambridge, MA 02139, USA

¹⁵Kavli fellow

¹⁶NASA Goddard Space Flight Center, 8800 Greenbelt Rd, Greenbelt, MD 20771, USA

¹⁷University of Maryland, Baltimore County, 1000 Hilltop Cir, Baltimore, MD 21250, USA

¹⁸NASA Ames Research Center, Moffett Field, CA, 94035, USA

¹⁹Department of Earth, Atmospheric and Planetary Sciences, Massachusetts Institute of Technology, Cambridge, MA 02139, USA

²⁰Department of Aeronautics and Astronautics, MIT, 77 Massachusetts Avenue, Cambridge, MA 02139, USA

²¹University of Southern Queensland, Centre for Astrophysics, West Street, Toowoomba, QLD 4350 Australia

²²Department of Astronomy, The University of Texas at Austin, TX 78712, USA

²³Department of Physics, Massachusetts Institute of Technology, Cambridge, MA, USA

²⁴Department of Earth and Planetary Sciences, University of California, Riverside, CA 92521, USA

²⁵Department of Physics and Astronomy, University of Louisville, Louisville, KY 40292, USA

²⁶Department of Astronomy, University of Florida, 211 Bryant Space Science Center, Gainesville, FL, 32611, USA

²⁷Department of Physics and Astronomy, George Mason University, 4400 University Drive MS 3F3, Fairfax, VA 22030, USA

²⁸Exoplanetary Science at UNSW, School of Physics, UNSW Sydney, NSW 2052, Australia

²⁹School of Physics and Astronomy, Tel Aviv University, Tel Aviv 69978, Israel

³⁰Las Cumbres Observatory Global Telescope Network, Santa Barbara, CA 93117, USA

³¹Department of Physics, University of California, Santa Barbara, CA 93106-9530, USA

³²Dunlap Institute for Astronomy and Astrophysics, University of Toronto, 50 St. George Street, Toronto, Ontario M5S 3H4, Canada

³³Department of Physics and Astronomy, The University of North Carolina at Chapel Hill, Chapel Hill, NC 27599-3255, USA

(Received; Revised; Accepted)

Submitted to AAS

ABSTRACT

We report the discovery of TOI-677 b, first identified as a candidate in light curves obtained within Sectors 9 and 10 of the Transiting Exoplanet Survey Satellite (*TESS*) mission and confirmed with radial velocities. TOI-677 b has a mass of $M_p = 1.236^{+0.069}_{-0.067} M_J$, a radius of $R_p = 1.170 \pm 0.03 R_J$, and orbits its bright host star ($V = 9.8$ mag) with an orbital period of 11.23660 ± 0.00011 d, on an eccentric orbit with $e = 0.435 \pm 0.024$. The host star has a mass of $M_\star = 1.181 \pm 0.058 M_\odot$, a radius of $R_\star = 1.28^{+0.03}_{-0.03} R_\odot$, an age of $2.92^{+0.80}_{-0.73}$ Gyr and solar metallicity, properties consistent with a main sequence late F star with $T_{\text{eff}} = 6295 \pm 77$ K. We find evidence in the radial velocity measurements of a secondary long term signal which could be due to an outer companion. The TOI-677 b system is a well suited target for Rossiter-McLaughlin observations that can constrain migration mechanisms of close-in giant planets.

Keywords: planetary systems – stars: individual: TOI-677 – planets and satellites: gaseous planets – planets and satellites: detection

1. INTRODUCTION

In the past two decades the population of known transiting exoplanets has grown at an accelerating pace. While the *Kepler* satellite (Borucki et al. 2010) dominates the overall number of discoveries, the particular class of close-in gas giants around nearby stars were until recently most efficiently discovered by wide-field photometric series (e.g. Bakos et al. 2004; Pollacco et al. 2006; Pepper et al. 2007; Bakos et al. 2013; Talens et al. 2017). Due to the biases inherent to ground based observatories, most of the discoveries of these surveys have periods $P \lesssim 10$ d. Systems of stations around the globe such as the HATSouth survey can in principle improve the efficiency of discovery for longer periods, but the number of systems with $P > 10$ d uncovered by wide-field ground-based surveys is small, with the current record holder being HATS-17b with $P \approx 16$ d (Brahm et al. 2016).

The population of close-orbiting gas giants has opened a number of questions about their physical structural and dynamical evolution which are still topics of active research (Dawson & Johnson 2018). In particular, the nature of the migration history and the detailed mechanism of radius inflation for hot Jupiters need further elucidation. In order to make further progress on those fronts the population of *warm* giants, loosely defined as systems with periods $P \gtrsim 10$ d, is of importance. They are close enough to the star that they are likely to have undergone significant migration, but not as close that tidal effects can erase the potential imprints of that migration (Albrecht et al. 2012; Dawson 2014; Li & Winn 2016). In the same vein, they are far enough from their parent star that their radii have not been inflated by the mechanism that acts to bloat the radii of hotter giants (Kovács et al. 2010; Demory & Seager 2011; Miller & Fortney 2011). But while it is clear that these systems are very interesting, the population of known warm

giants around nearby stars (allowing the most detailed characterization) is still very small. The launch of the *TESS* mission (Ricker et al. 2015) is changing that. By scanning nearby stars around the whole sky the expectation is that hundreds of giant planets with $P \gtrsim 10$ d will be uncovered (Sullivan et al. 2015; Barclay et al. 2018).

In this work we present the discovery originating from a *TESS* light curve of an eccentric warm giant planet with a period of $P = 11.23660 \pm 0.00011$ days orbiting a bright late F star. This is part of a systematic effort to characterize warm giants in the southern hemisphere uncovered with *TESS* which has contributed to the discovery and mass measurement of three warm giants already (Brahm et al. 2019; Huber et al. 2019; Rodriguez et al. 2019). The paper is structured as follows. In § 2 we describe the observational material which gets used to perform a global modeling of the system as described in § 3. The results are then discussed in § 4.

2. OBSERVATIONS

2.1. *TESS*

Between 2019 March 01 and 2019 April 22, the *TESS* mission observed TOI-677 (TIC 280206394, 2MASS J09362869-5027478, TYC 8176-02431-1, WISE J093628.65-502747.3) during the monitoring of Sectors 9 and 10, using camera 3 and CCDs 1 and 2, respectively. The *TESS* Science Processing Operations Center (SPOC; for an overview of the processing it carries out see Jenkins et al. 2016) Transiting Planet Search module detected the planetary signature in the Sector 9 processing run and in the Sectors 1-13 multi-sector search and triggered the Data Validation module (Twicken et al. 2018; Li et al. 2019) to analyze the transit-like feature in the Sector 9 and combined Sectors 9 and 10 light curves. All diagnostics tests performed as part of the data validation report, including the odd/even depth

test, the signal to noise ratio, the impact parameter, the statistical bootstrap probability, the ghost diagnostic, and the difference image centroid offset from the TIC position and from the out-of-transit centroid, strongly favored the planetary hypothesis and resulted in the promotion of TOI-677 to the list of targets of interest.

The properties of TOI-677 as obtained from literature sources and derived in this work are detailed in Table 1. The target was observed in short (2 min) cadence, and we downloaded the PDC (Pre-search Data Conditioning) SAP light curves from the Mikulski Archives for Space Telescopes. The PDC SAP light curves have systematic trends removed by the use of co-trending basis vectors (Smith et al. 2012; Stumpe et al. 2014), and are produced by the TESS SPOC at NASA Ames Research Center. We masked the regions of high scattered light as indicated in the data release notes for each of the sectors, augmenting the masked windows in a few cases where it was evident that there were some remaining trends that were insufficiently masked¹. We did not mask datapoints with data quality flags, as we noticed that all of the second transit had been masked with a flag value of 2048 (stray light from Earth or Moon in camera field of view), but inspection of the masked portions revealed no anomalous signs on the light curve.

The TESS light curve is shown in Figure 1, where four transits are clearly seen. The out-of-transit light curve is remarkably flat. We estimated the power spectral density of the out-of-transit light curve of TOI-677 using the method of Welch (1967) as implemented in the `scipy.signal` Python module and found it to be featureless and at precisely the level expected given the reported photometric uncertainties of the magnitude measurements (see Figure 2). We conclude from this exercise that there is no need for any deterministic or stochastic component beyond the white noise implied by the photometric uncertainties in the modeling of the out-of-transit light curve. Because of this we only fit for regions of $\approx 1d$ around each transit, removing the median value calculated in the out-of-transit portion for each transit. The TESS data used for the analysis is presented in Table 4

2.2. Spectroscopy

We followed up TOI-677 with several spectrographs in order to confirm the TESS transiting planet candidate and to measure its mass. In what follows we describe

¹ In detail, in the first and second orbits of sector 10 we excluded up to cadence numbers 247000 and 257300, respectively, instead of the values 246576 and 256215 indicated in the data release notes for sector 10.

the observations obtained by each spectrograph we used. The derived radial velocities, and bisector span measurements when available, are reported in Table 5.

2.2.1. FEROS

TOI-677 was monitored with the FEROS spectrograph ($R \approx 48000$, Kaufer et al. 1999) mounted at the MPG 2.2m telescope at La Silla Observatory between May and July of 2019, where 26 spectra were obtained. Observations were performed in simultaneous calibration mode, with the secondary fibre observing a thorium-argon (ThAr) lamp to trace the instrumental variations produced by changes in the environment during the science exposures. The adopted exposure times were of 300 s and 400 s, which translated into a signal-to-noise ratio ranging between 40 and 150 per resolution element. The FEROS data were processed with the CERES pipeline (Brahm et al. 2017a), which delivers the radial velocities corrected by the instrumental drift variations and the by the Earth's motion. These radial velocities were obtained with the cross-correlation technique, where a G2-type binary mask was used as template. From this cross-correlation peak CERES also computes the bisector span measurements, and delivers a rough estimate of the stellar parameters by comparing the continuum normalized spectrum with a grid of synthetic ones.

2.2.2. Coralie

We monitored TOI-677 with the Coralie spectrograph ($R \approx 60000$, Mayor et al. 2003) mounted on the Swiss-Euler 1.2m telescope in six different epochs. These observations were also performed with the simultaneous calibration technique, but in this case the secondary fibre is illuminated by a Fabry-Perot etalon. We adopted an exposure time of 300 s, which produced spectra having a typical signal-to-noise ratio of 30 per resolution element. Coralie data were also processed with the CERES pipeline for obtaining the radial velocities.

2.2.3. CHIRON

We collected a total of 11 spectra of TOI-677 using the CHIRON high-resolution spectrograph (Tokovinin et al. 2013), between May 17 and June 19, 2019. The exposure time was between 750–1200 s, leading to a signal-to-noise ratio (SNR) per pixel between ≈ 20 -35. CHIRON is mounted on the SMARTS 1.5 m telescope at the Cerro Tololo Inter-American observatory in Chile, and is fed by an octagonal multi-mode optical fibre. For these observations we used the image slicer, which delivers relatively high throughput and high spectral resolution ($R \approx 80,000$). The radial velocities were computed from the

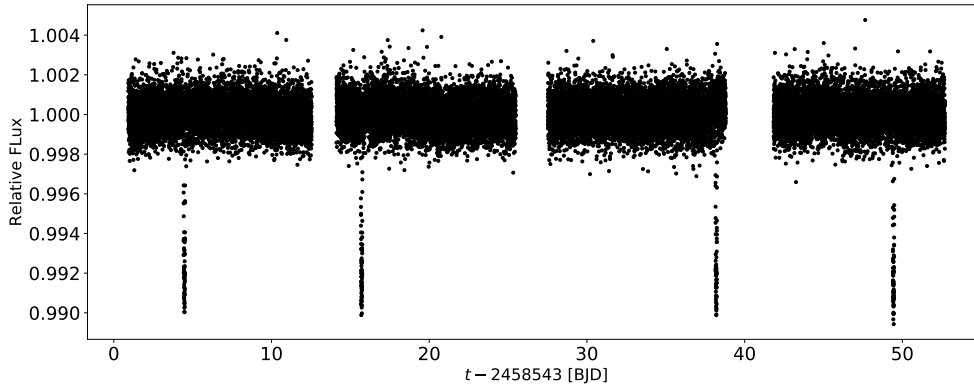


Figure 1. The 2 min cadence TESS light curve. These are the PDC SAP measurements produced by the SPOC pipeline. Four transits are clearly seen in the TESS photometry, with the middle transit falling within a gap.

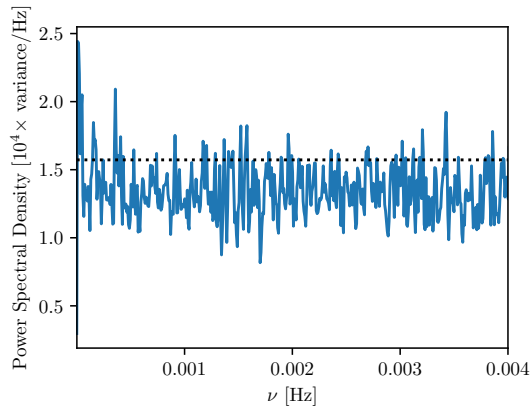


Figure 2. Power spectral density of the out-of-transit TESS light curve. The dashed line marks the expected value of the power spectral density, estimated as $\langle \sigma_i^2 \rangle / (\nu_u - \nu_l)$, where $\langle \sigma_i^2 \rangle$ is the average measurement variance of the TESS photometry, $\nu_l = 0$ and $\nu_u \approx 0.004$ Hz is the Nyquist frequency for the short cadence sampling.

cross-correlation function between the individual spectra and a high-resolution template of the star, which is built by stacking all individual observations of this star. Since CHIRON is not equipped with a simultaneous calibration, we observed the spectrum of a Th-Ar lamp before the science observations, to correct for the instrumental drift. Using this method we have measured a long-term RV stability of $< 10 \text{ m s}^{-1}$ on bright targets ($t_{exp} < 60$ s) and $< 15 \text{ m s}^{-1}$ for fainter objects ($t_{exp} < 1800$ s). For more details of the method see Wang et al. (2019) and Jones et al. (2019).

2.2.4. NRES

NRES (Sivervd et al. 2018) is a global array of echelle spectrographs mounted on 1-meter telescopes, with a resolving power of $\approx 53,000$. TOI-677 was observed at 12 epochs with the NRES node located at the Cerro

Tololo Inter-American Observatory. At each observing epoch, three consecutive 1200 s exposures were obtained, with individual signal-to-noise ratio $\gtrsim 40$. The velocity of each exposure was derived via cross-correlation with a PHOENIX template (Husser et al. 2013) with $T_{\text{eff}}=5800$ K, $\log g=3.5$, $[\text{Fe}/\text{H}]=-0.5$ and $v \sin i=7$ km/s. Systematic drifts were corrected per order (e.g., Engel et al. 2017) and the radial velocity of each epoch was then taken as the mean of the three exposures.

2.2.5. Minerva-Australis

We obtained 17 observations on nine separate nights with the MINERVA-Australis telescope array (Addison et al. 2019) at Mount Kent Observatory in Queensland, Australia. All of the telescopes in the MINERVA-Australis array simultaneously feed a single Kiwispec R4-100 high-resolution ($R \approx 80,000$) spectrograph with wavelength coverage from 500 to 630 nm over 26 echelle orders. We derived radial velocities for each telescope using the least-squares analysis of Anglada-Escudé & Butler (2012) and corrected for spectrograph drifts with simultaneous Thorium-Argon arc lamp observations. TOI-677 was observed with telescopes 3, 4 and 5 of the array, the derived radial velocities are reported under the instrument labels Minerva_T3, Minerva_T4 and Minerva_T5 in Table 5.

2.3. Ground-based photometry

2.3.1. Shared Skies Telescope at Mt. Kent Observatory (SSMKO)

TOI-677 was observed on the night of UTC 2019-05-09 with the University of Louisville’s Shared Skies MKO-CDK700 (SSMKO) telescope at Mt. Kent Observatory of the University of Southern Queensland, Australia. The telescope is a 0.7-meter corrected Dall-Kirkham with a Nasmyth focus manufactured by Planewave. Images with an exposure time of 64 s were taken through

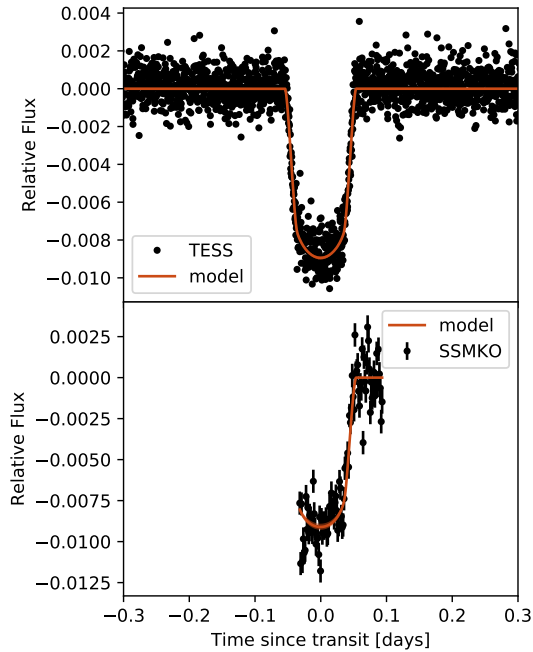


Figure 3. Photometric data with the trend subtracted as a function of phase for the two photometric instruments used in this work (TESS, SSMKO). The orange line shows the posterior transit model.

a Sloan i' filter using an Apogee U16 CCD camera with a Kodak KAF-16801E sensor. A sequence of 92 images were acquired over 180 minutes. The light curve, which is shown in Figure 3 displays a clear egress. No significant activity or modulation other than the transit itself was apparent in the light curve, which shows residuals of 0.85 ppt at the observational cadence. The SSMKO data used for the analysis is presented in Table 4

2.4. Gaia DR2

Observations of TOI-677 by Gaia were reported in DR2 (Gaia Collaboration et al. 2016, 2018). From GAIA DR2, TOI-677 has a parallax of 7.02 ± 0.03 mas, an effective temperature of $T_{\text{eff}} = 5895^{+105}_{-200}$ K and a radius of $R_{\star} = 1.37^{+0.1}_{-0.05} R_{\odot}$. The parallax obtained from GAIA was used to determine the stellar physical parameters of TOI-677 as described in Section 3.1. In our analysis we corrected the GAIA DR2 parallax for the systematic offset of $-82 \mu\text{as}$ reported in Stassun & Torres (2018).

2.5. High spatial resolution imaging

The relatively large angle subtended by the TESS pixels, approximately $21''$ on a side, leave it susceptible to photometric contamination from nearby stars, including additional wide stellar companions. We searched for nearby sources to TIC 280206394 with SOAR speckle imaging (Tokovinin 2018) on 18 May 2019 UT, observ-

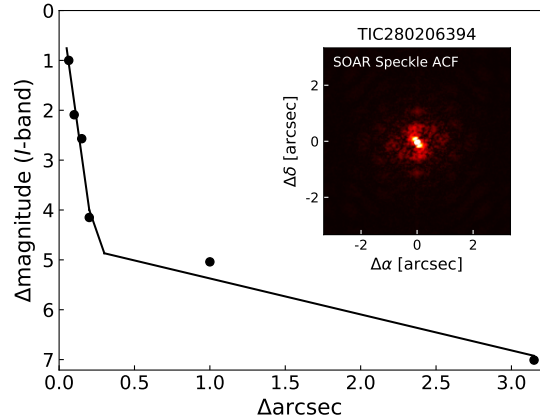


Figure 4. The I -band auto-correlation function from Speckle using SOAR. The $5\text{-}\sigma$ contrast curve for TOI-677 is shown by the black points. The black solid line is the linear fit to the data for separations $< 0''.2$ and $> 0''.2$. The auto-correlation function is shown within the contrast curve plot.

ing through a similar visible bandpass as TESS. More details of these observations are available in Ziegler et al. (2019). We detected no nearby sources within $3''$ of TIC 280206394. The 5σ detection sensitivity and the speckle auto-correlation function from the SOAR observation are plotted in Figure 4.

The radial velocity variations measured on TOI-677 phase with the transit signal. This fact, combined with the lack of nearby companions, the lack of correlation of the bisector span measurements with orbital phase and the tests carried out as part of the SPOC data validation report show that the transit is not caused by a blended stellar eclipsing binary.

3. ANALYSIS

3.1. Stellar parameters

In order to characterize the star, we follow the same procedure presented in Brahm et al. (2019). First, we compute the stellar atmospheric parameters using the co-added FEROS spectra through the ZASPE code (Brahm et al. 2017b). ZASPE estimates T_{eff} , $\log g$, $[\text{Fe}/\text{H}]$, and $v \sin i$, by comparing an observed spectrum with a grid of synthetic models generated with the ATLAS9 atmospheres (Castelli & Kurucz 2004).

Then, we estimate the physical parameters of the host star using the publicly available broadband photometry of GAIA (G, B_P , R_P) and 2MASS (J, H, K_S), which is compared to the synthetic magnitudes provided by the PARSEC stellar evolutionary models by using the distance to the star from the Gaia DR2 parallax. For a given stellar mass, age and metallicity, the PARSEC models can deliver a set of synthetic absolute magni-

tudes and other stellar properties (e.g. stellar luminosity, effective temperature, stellar radius).

We determine the posterior distributions for M_* , Age, and A_V , via an MCMC code using the `emcee` package (Foreman-Mackey et al. 2013), where we fix the metallicity of the PARSEC models to that obtained with ZASPE, and we apply the Cardelli et al. (1989) extinction laws to the synthetic magnitudes.

This procedure provides a more precise estimation of $\log g$ than the one obtained from the spectroscopic analysis. For this reason we iterate the procedure where we fix the $\log g$ value when running ZASPE to the value obtained from the PARSEC models. The resulting values are $T_{\text{eff}} = 6295 \pm 77$ K, $[\text{Fe}/\text{H}] = 0.00 \pm 0.05$ dex, $\log g = 4.291 \pm 0.025$, $v \sin i = 7.80 \pm 0.19$ km s $^{-1}$, $A_V = 0.226_{-0.058}^{+0.056}$ mag, age = $2.92_{-0.73}^{+0.80}$ Gyr, $L_* = 2.33 \pm 0.11 L_\odot$, $M_* = 1.170 \pm 0.06 M_\odot$ and $R_* = 1.282 \pm 0.03 R_\odot$. The values and uncertainties of M_* and R_* are used to define priors for them in the global analysis described in the next section.

3.2. Global modeling

We performed joint modelling of the radial velocity and photometric data using the `exoplanet` toolkit (Foreman-Mackey et al. 2019). The radial velocities used are given in Table 5 and the photometric data are given in Table 4. We denote the TESS photometric time series by $\{y_T(t_i)\}_{i=1}^{n_T}$, the SSMKO one by $\{y_S(t_i)\}_{i=1}^{n_S}$, and the radial velocity measurements (with their mean values removed) by $\{y_F(t_i)\}_{i=1}^{n_F}$, $\{y_C(t_i)\}_{i=1}^{n_C}$, $\{y_\chi(t_i)\}_{i=1}^{n_\chi}$, $\{y_N(t_i)\}_{i=1}^{n_N}$ and $\{y_{M(i)}(t_i)\}_{i=1}^{n_{M(i)}}$ for FEROS, Coralie, CHIRON, NRES, and Minerva Australis respectively. In the case of Minerva, $M(i)$ is a function that returns the telescope used at observation t_i (recall the Minerva observations include three different telescopes). The observational uncertainties are denoted by $\sigma_*(t_i)$, where $*$ can take the value of any of the instrument labels. As shown in § 2.1, the TESS light curve shows no evidence of additional structure beyond white noise. The TESS photometric time series is therefore modeled as

$$y_T(t_i) = \mathcal{T}(t_i; \mathbf{p}) + N(0, \sigma_{T,i}^2), \quad (1)$$

where $N(0, \sigma^2)$ denotes a Normal distribution of mean 0 and variance σ^2 , $\mathcal{T}(t_i; \mathbf{p})$ is the transit model, and \mathbf{p} is the vector of model parameters. Explicitly,

$$\mathbf{p} = (R_p, b, P, t_0, e, \omega, R_*, M_*, u_1, u_2), \quad (2)$$

where R_p is the planetary radius, b is the impact parameter, P is the period, t_0 the reference time of mid-transit, e the eccentricity, ω the angle of periastron, R_*

and M_* the stellar radius and mass, and u_1 and u_2 the limb-darkening law coefficients, which we describe using a quadratic law.

The SSMKO photometric time series is modeled as

$$\begin{aligned} y_S(t_i) &= \mathcal{T}(t_i; \mathbf{p}_u) + N(0, \sigma_{S,i}^2 + \eta_S^2) \\ &+ b_0 + b_1(t_i - t_0) \\ &\equiv \phi_S(t_i) + N(0, \sigma_{S,i}^2), \end{aligned} \quad (3)$$

where the $\{b_i\}$ coefficients accounts for up to a linear systematic trend in the photometry, $\sigma_{S,i}^2$ are the reported photometric uncertainties, and η_S is an additional photometric variance parameter. The parameter vector is the same as that for TESS, but the limb darkening coefficients are fixed to the values $(u_1, u_2) = (0.2489, 0.305)$. These values were calculated using the ATLAS atmospheric models and the Sloan i' band using the limb darkening coefficient calculator (Espinoza & Jordán 2015), and in particular using the methodology of sampling the limb darkening profile in 100 points as described in Espinoza & Jordán (2015). We chose to fix the limb darkening coefficients given that the SSMKO light curve covers only the egress. The radial velocity times series are modeled as

$$\begin{aligned} y_*(t_i) &= \mathcal{O}(t_i; \mathbf{q}) + N(0, \sigma_{*,i}^2 + \eta_*^2) + \gamma_* \\ &a_0 + a_1(t - t_0) \\ &\equiv r_*(t_i) + N(0, \sigma_{*,i}^2 + \eta_*^2) \end{aligned} \quad (4)$$

where \mathcal{O} represents the Keplerian radial velocity curve and the parameter vector of the model, a subset of \mathbf{p} , is $\mathbf{q} = (P, t_0, e, \omega, M_*)$. The wildcard $*$ can take the values F, C, χ, N, M for FEROS, Coralie, CHIRON, NRES and Minerva respectively, and η_*^2 is a white noise ‘‘jitter’’ terms to account for additional variance not accounted for in the observational uncertainties. The parameters a_i account for up to a linear systematic trend in the radial velocities. We set priors for η_*^2 by first running a model without jitter terms, and determining for each instrument how much extra variance was present around the posterior model over that predicted by the observational uncertainties. We note that for NRES we found no need for a jitter term and thus we set $\eta_N \equiv 0$. The log-likelihood l is given by

Table 1. Stellar properties of TOI-677

| Parameter | Value | Reference |
|--|--|-----------|
| Names | TIC 280206394 | TIC |
| | 2MASS J09362869-5027478 | 2MASS |
| | TYC 8176-02431-1 | TYCHO |
| | WISE J093628.65-502747.3 | WISE |
| RA .. (J2000) | 15h32m17.84s | |
| DEC . (J2000) | -22d21m29.74s | |
| μ_α (mas yr ⁻¹) | -24.82 ± 0.05 | Gaia |
| μ_δ (mas yr ⁻¹) | 42.42 ± 0.05 | Gaia |
| π (mas) | 7.02 ± 0.03 | Gaia |
| TESS .. (mag) | 9.24 ± 0.018 | TIC |
| G (mag) | 9.661 ± 0.020 | Gaia |
| B _P (mag) | 9.968 ± 0.005 | Gaia |
| R _P (mag) | 9.229 ± 0.003 | Gaia |
| J (mag) | 8.722 ± 0.020 | 2MASS |
| H (mag) | 8.470 ± 0.038 | 2MASS |
| K _s (mag) | 8.429 ± 0.023 | 2MASS |
| T_{eff} (K) | 6295 ± 77 | zaspe |
| log g (dex) | 4.291 ± 0.025 | zaspe |
| [Fe/H] .. (dex) | 0.00 ± 0.05 | zaspe |
| $v \sin i$ (km s ⁻¹) | 7.80 ± 0.19 | zaspe |
| M_\star (M _⊙) | 1.181 ± 0.058 | this work |
| R_\star (R _⊙) | 1.28 ^{+0.03} _{-0.03} | this work |
| Age (Gyr) | 2.92 ^{+0.80} _{-0.73} | this work |
| ρ_\star ... (g cm ⁻³) | 0.80 ^{+0.06} _{-0.06} | this work |

$$\begin{aligned}
-2l(\mathbf{p}) = & \sum_{i=1}^{n_T} \sigma_{T,i}^{-2} (y_{T,i} - \mathcal{T}_{T,i})^2 \\
& + \sum_{i=1}^{n_S} (\sigma_{S,i}^2 + \eta_S^2)^{-2} (y_{S,i} - \phi_{S,i})^2 + \ln(\sigma_{S,i}^2 + \eta_S^2) \\
& + \sum_{i=1}^{n_F} (\sigma_{F,i}^2 + \eta_F^2)^{-2} (y_{F,i} - r_{F,i})^2 + \ln(\sigma_{F,i}^2 + \eta_F^2) \\
& + \sum_{i=1}^{n_C} (\sigma_{C,i}^2 + \eta_C^2)^{-2} (y_{C,i} - r_{C,i})^2 + \ln(\sigma_{C,i}^2 + \eta_C^2) \\
& + \sum_{i=1}^{n_X} (\sigma_{X,i}^2 + \eta_X^2)^{-2} (y_{X,i} - r_{X,i})^2 + \ln(\sigma_{X,i}^2 + \eta_X^2) \\
& + \sum_{i=0}^{n_M} (\sigma_{M(i),i}^2 + \eta_M^2)^{-2} (y_{M,i} - r_{M(i),i})^2 + \ln(\sigma_{M(i),i}^2 + \eta_M^2) \\
& + \sum_{i=1}^{n_N} \sigma_{N,i}^{-2} (y_{N,i} - r_{N,i})^2. \tag{5}
\end{aligned}$$

Posteriors were sampled using an Monte Carlo Markov Chain algorithm, specifically the No U-Turn Sampler (NUTS, Hoffman & Gelman 2011) as implemented in the PyMC3 package through `exoplanet`. We sampled using 4 chains and 3000 draws, after a tuning run of 4500 draws where the step sizes are optimized. Convergence was verified using the Rubin-Gelman and Geweke statistics. The effective sample size for all parameters, as defined by (Gelman et al. 2013), was > 4000 . The priors are detailed in Table 2. Priors for M_* and R_* stem from the analysis described in § 3.1. The priors on P , T_0 , $\ln(M_p/mM_\oplus)$, e , $\{a_i\}_{i=0}^1$ were obtained from a fit to the radial velocities alone carried out with the `radvel` package (Fulton et al. 2018).

The posterior model for the radial velocities is shown in Figure 5 as a function of time and in Figure 6 against orbital phase with the quadratic term removed. The posterior model for the photometric observations is shown in Figure 3. Table 2 lists all the priors assumed and the posterior values for the stellar and planetary properties. A fully independent analysis of the data with the `juliet` package (Espinoza et al. 2018) using different priors and treatment of photometric and radial velocity trends results in planetary parameters consistent with the ones presented in Table 2. It is noteworthy that besides the Keplerian orbit, there is significant statistical evidence for a long term trend in the radial velocities which could be caused by an outer companion. If described by a linear trend the slope is estimated to be $a_1 = 1.58 \pm 0.19 \text{ m s}^{-1} \text{ d}^{-1}$.

4. DISCUSSION

We put TOI-677 b in the context of the population of known, well characterized² transiting exoplanets in Figure 7, where we show a scatter plot of planetary mass versus planetary radius, coding with color the equilibrium temperature. The incident flux for TOI-677 b is $\approx 3 \times 10^8 \text{ erg s}^{-1} \text{ cm}^{-2}$, very close to the value of $\approx 2 \times 10^8 \text{ erg s}^{-1} \text{ cm}^{-2}$ below which it has been shown that the effects of irradiation on the planetary radius are negligible (e.g. Demory & Seager 2011). The radius of TOI-677 b is in line with what is expected for a gas giant with a core of $M_C = 10M_\oplus$ according to the standard models of Fortney et al. (2007). This underscores the value of warm giants, whose structure can be modeled without the complications of an incident flux resulting in radius inflation (Kovács et al. 2010; Demory & Seager 2011). Figure 7 also shows that TOI-677 b, having a transmission spectroscopy metric (TSM, Kempton et al. 2018) of ≈ 100 , is not a particularly well suited target of transmission spectroscopy studies, if compared with the rest of the population of close-in giant planets.

In Figure 8 we plot the same population of well-characterized planets in the period–eccentricity plane, coding the planetary mass with the symbol size. It is apparent that TOI-677 b lies in a part of this plane that is still sparsely populated. The eccentricity of exoplanets is very low for close-in systems, and starts to grow for periods $P \gtrsim 4 \text{ d}$. With an eccentricity of $e = 0.435 \pm 0.024$, TOI-677 b lies in the upper range of eccentricity values for planets with similar periods in the currently known sample. Besides the significant eccentricity of the orbit of TOI-677 b the presence of a long term trend in the radial velocities is interesting in the context of migration mechanisms of giant planets. Warm jupiters can be formed via secular gravitational interactions with an outer planet followed by tidal interactions with the star in the high eccentricity stage of the secular cycle (e.g. Kozai 1962). In this context, Dong et al. (2014) predicts that in order to overcome the precession caused by general relativity, the warm jupiters produced via this mechanism should have outer planets at relatively short orbital distances that can be detected with a radial velocity monitoring. At the moment we cannot provide meaningful constraints on a potential outer companion. We will continue to monitor the system with radial velocities to determine the exact nature of the long term radial velocity we uncovered.

² We use the catalog of well characterized planets of (Southworth 2011). We restrict the sample to systems whose fractional error on their planetary masses and radii are $< 25\%$.

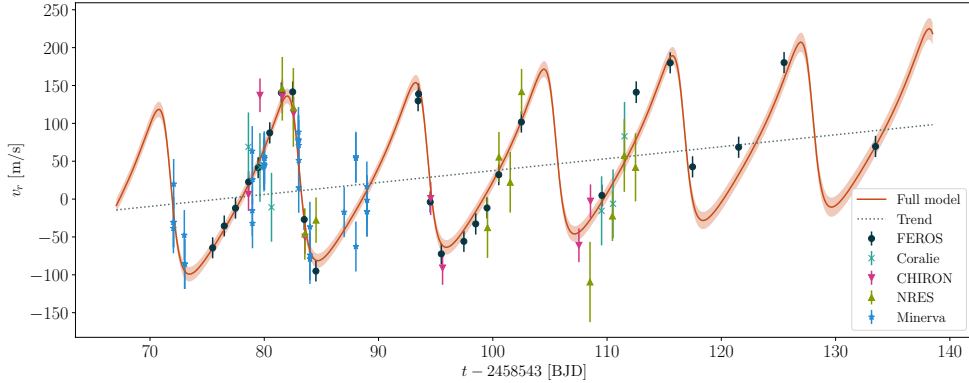


Figure 5. Radial velocities as a function of time for the five spectroscopic instruments used in this work (FEROS, Coralie, CHIRON, NRES, Minerva). Note that we use a single symbol for Minerva but the observations were made with three different telescopes in the array. The error bars include the posterior values for the jitter terms.

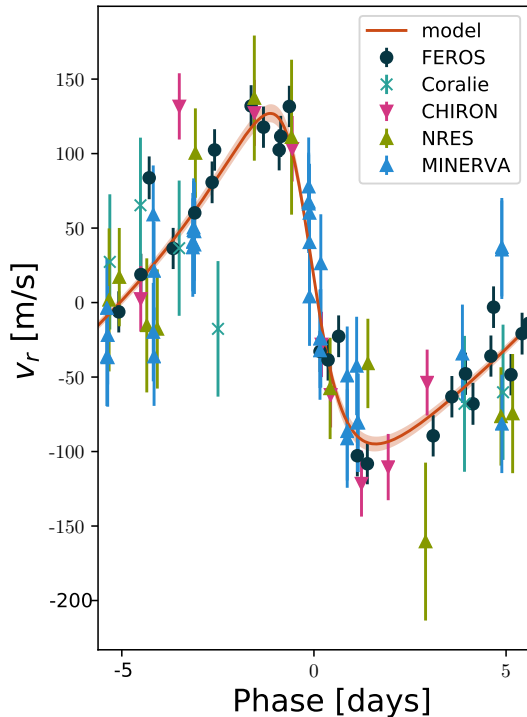


Figure 6. Radial velocities as a function of orbital phase for the five spectroscopic instruments used in this work (FEROS, Coralie, CHIRON, NRES, Minerva). Note that we use a single symbol for Minerva but the observations were made with three different telescopes in the array. The error bars include the posterior values for the jitter terms.

The determination of the orbital obliquity of transiting planets through the Rossiter-McLaughlin (R-M) effect, particularly for planets with orbital periods longer than ≈ 10 days, provides a powerful tool to constrain migration theories (Petrovich & Tremaine 2016). With a sizable $v \sin i$ of $7.80 \pm 0.19 \text{ km s}^{-1}$ and a bright mag-

nitude of $V = 9.8$ mag, TOI-677 b is a prime target to perform a measurement of the projected angle between the stellar and orbital angular momenta. Specifically, the expected semi-amplitude of the R-M signal for TOI-677 b in the case of an aligned orbit is of $K_{R-M} = 70 \pm 10 \text{ ms}^{-1}$. While still based on a very limited population, the current obliquity distribution of transiting planets with similar periods as TOI-677 b seems to follow a similar behaviour to that of the eccentricity distribution, with a large spread in their values. Current discoveries include aligned systems like WASP-84b (Anderson et al. 2015) and HAT-P-17b (Fulton et al. 2013), mildly misaligned systems (WASP-117b, Lendl et al. 2014), and also others that are even retrograde (WASP-8b, Queloz et al. 2010). The measurement of the obliquity of TOI-677 b will increment this small sample and help in further understanding how close-in giant planets form.

A.J. acknowledges support from FONDECYT project 1171208 and by the Ministry for the Economy, Development, and Tourism’s Programa Iniciativa Científica Milenio through grant IC120009, awarded to the Millennium Institute of Astrophysics (MAS). R.B. acknowledges support from FONDECYT Post-doctoral Fellowship Project 3180246, and from the Millennium Institute of Astrophysics (MAS). M.B. acknowledges CONICYT-GEMINI grant 32180014. T.D. acknowledges support from MITs Kavli Institute as a Kavli postdoctoral fellow. Resources supporting this work were provided by the NASA High-End Computing (HEC) Program through the NASA Advanced Supercomputing (NAS) Division at Ames Research Center for the production of the SPOC data products. This work has made use of data from the European Space Agency (ESA) mission Gaia (<https://www.cosmos.esa.int/gaia>), processed

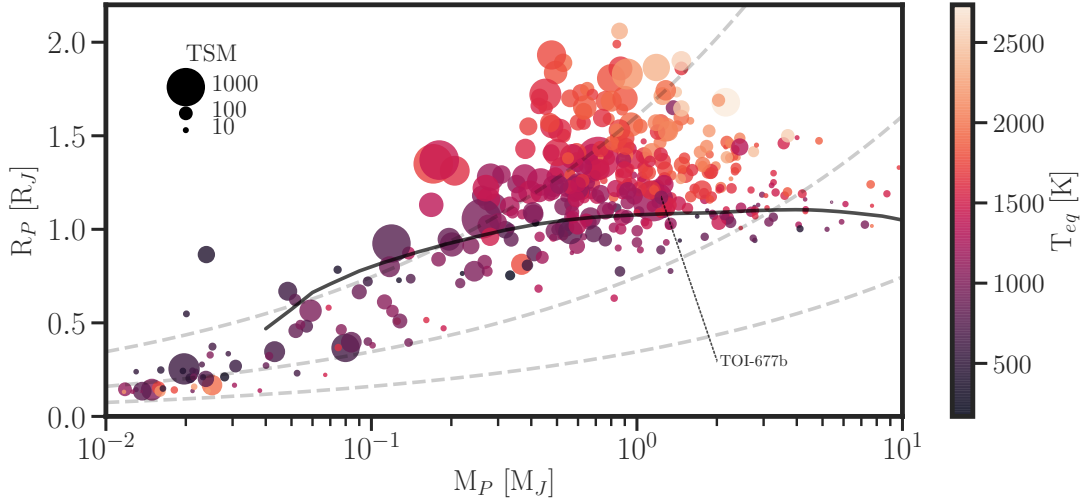


Figure 7. Mass – Radius diagram for the population of well characterized transiting planets (Southworth 2011). The point corresponding to TOI-677 b is indicated with a dashed line. The color represents the equilibrium temperature of the planet, while the size scales down with the transmission spectroscopy metric as defined by Kempton et al. (2018). The dashed gray lines correspond to isodensity curves for 0.3, 3 and 30 g cm^{-3} , respectively. The solid line corresponds to the predicted radius using the models of Fortney et al. (2007) for a planet with a 10 M_\oplus central core.

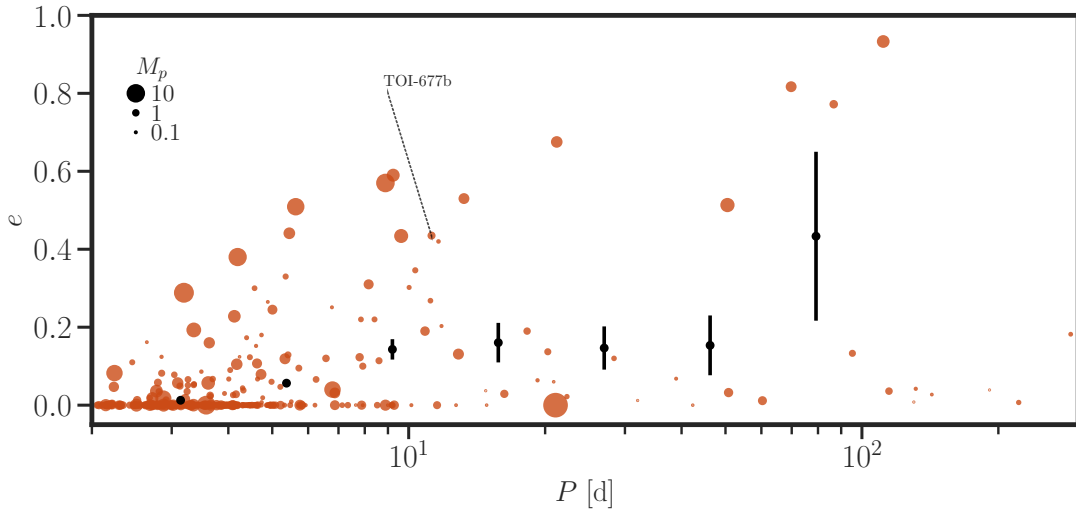


Figure 8. Period – Eccentricity diagram for the population of well characterized transiting planets. The point corresponding to TOI-677 b is indicated with a dashed line. The size scales with the mass of the planet. The black points with error bars are the average eccentricities of the sample in bins that are equally spaced in $\log(P)$ for $P < 100$ d.

by the Gaia Data Processing and Analysis Consortium (DPAC, <https://www.cosmos.esa.int/web/gaia/dpac/consortium>). Funding for the DPAC has been provided by national institutions, in particular the institutions participating in the Gaia Multilateral Agreement. This research made use of exoplanet (Foreman-Mackey et al. 2019) and its dependencies (Astropy Collaboration et al.

2013, 2018; Espinoza 2018; Foreman-Mackey et al. 2019; Kipping 2013; Luger et al. 2019; Salvatier et al. 2016; Theano Development Team 2016). MINERVA-Australis is supported by Australian Research Council LIEF Grant LE160100001, Discovery Grant DP180100972, Mount Cuba Astronomical Foundation, and institutional partners University of Southern Queensland,

UNSW Australia, MIT, Nanjing University, George Mason University, University of Louisville, University of California Riverside, University of Florida, and The University of Texas at Austin. We respectfully acknowledge the traditional custodians of all lands throughout Australia, and recognise their continued cultural and spiritual connection to the land, waterways, cosmos, and community. We pay our deepest respects to all Elders, ancestors and descendants of the Gabal, Jarowair, and Kambuwal nations, upon whose lands the Minerva-Australis facility at Mt. Kent is situated.

Facilities: TESS, FEROS/MPG2.2m, Coralie/Euler1.3m, NRES/LCOGT1m, Minerva Australis, Shared Skies Telescope/Mount Kent Observatory, CTIO 1.5m/CHIRON

Software: CERES (Brahm et al. 2017a; Jordán et al. 2014), ZASPE (Brahm et al. 2017b, 2015), radvel (Fulton et al. 2018), exoplanet (Foreman-Mackey et al. 2019), juliet (Espinoza et al. 2018)

REFERENCES

- Addison, B., Wright, D. J., Wittenmyer, R. A., et al. 2019, arXiv e-prints, arXiv:1901.11231
- Albrecht, S., Winn, J. N., Johnson, J. A., et al. 2012, ApJ, 757, 18
- Anderson, D. R., TriAUD, A. H. M. J., Turner, O. D., et al. 2015, ApJL, 800, L9
- Anglada-Escudé, G., & Butler, R. P. 2012, ApJS, 200, 15
- Astropy Collaboration, Robitaille, T. P., Tollerud, E. J., et al. 2013, A&A, 558, A33
- Astropy Collaboration, Price-Whelan, A. M., Sipőcz, B. M., et al. 2018, AJ, 156, 123
- Bakos, G., Noyes, R. W., Kovács, G., et al. 2004, PASP, 116, 266
- Bakos, G. Á., Csubry, Z., Penev, K., et al. 2013, PASP, 125, 154
- Barclay, T., Pepper, J., & Quintana, E. V. 2018, ArXiv e-prints, arXiv:1804.05050
- Borucki, W. J., Koch, D., Basri, G., et al. 2010, Science, 327, 977
- Brahm, R., Jordán, A., & Espinoza, N. 2017a, PASP, 129, 034002
- Brahm, R., Jordán, A., Hartman, J., & Bakos, G. 2017b, MNRAS, 467, 971
- Brahm, R., Jordán, A., Hartman, J. D., et al. 2015, AJ, 150, 33
- Brahm, R., Jordán, A., Bakos, G. Á., et al. 2016, AJ, 151, 89
- Brahm, R., Espinoza, N., Jordán, A., et al. 2019, AJ, 158, 45
- Cardelli, J. A., Clayton, G. C., & Mathis, J. S. 1989, ApJ, 345, 245
- Castelli, F., & Kurucz, R. L. 2004, ArXiv e-prints, astro
- Dawson, R. I. 2014, ApJL, 790, L31
- Dawson, R. I., & Johnson, J. A. 2018, ArXiv e-prints, arXiv:1801.06117
- Demory, B.-O., & Seager, S. 2011, ApJS, 197, 12
- Dong, S., Katz, B., & Socrates, A. 2014, ApJL, 781, L5
- Engel, M., Shahaf, S., & Mazeh, T. 2017, Publications of the Astronomical Society of the Pacific, 129, 065002
- Espinoza, N. 2018, Research Notes of the American Astronomical Society, 2, 209
- Espinoza, N., & Jordán, A. 2015, MNRAS, 450, 1879
- Espinoza, N., Kossakowski, D., & Brahm, R. 2018, arXiv e-prints, arXiv:1812.08549
- Foreman-Mackey, D., Czekala, I., Agol, E., et al. 2019, dfm/exoplanet: exoplanet v0.2.0, , , doi:10.5281/zenodo.3359880. <https://doi.org/10.5281/zenodo.3359880>
- Foreman-Mackey, D., Hogg, D. W., Lang, D., & Goodman, J. 2013, PASP, 125, 306
- Fortney, J. J., Marley, M. S., & Barnes, J. W. 2007, ApJ, 659, 1661
- Fulton, B. J., Petigura, E. A., Blunt, S., & Sinukoff, E. 2018, ArXiv e-prints, arXiv:1801.01947
- Fulton, B. J., Howard, A. W., Winn, J. N., et al. 2013, ApJ, 772, 80
- Gaia Collaboration, Brown, A. G. A., Vallenari, A., et al. 2018, ArXiv e-prints, arXiv:1804.09365
- Gaia Collaboration, Prusti, T., de Bruijne, J. H. J., et al. 2016, A&A, 595, A1
- Gelman, A., Carlin, J., Stern, H., et al. 2013, Bayesian Data Analysis, Third Edition, Chapman & Hall/CRC Texts in Statistical Science (Taylor & Francis). <https://books.google.cl/books?id=ZXL6AQAQBAJ>
- Hoffman, M., & Gelman, A. 2011, Journal of Machine Learning Research, 15
- Huber, D., Chaplin, W. J., Chontos, A., et al. 2019, AJ, 157, 245
- Husser, T. O., Wende-von Berg, S., Dreizler, S., et al. 2013, Astronomy and Astrophysics, 553, A6
- Jenkins, J. M., Twicken, J. D., McCauliff, S., et al. 2016, in Proc. SPIE, Vol. 9913, Software and Cyberinfrastructure for Astronomy IV, 99133E

- Jones, M. I., Brahm, R., Espinoza, N., et al. 2019, *A&A*, 625, A16
- Jordán, A., Brahm, R., Bakos, G. Á., et al. 2014, *AJ*, 148, 29
- Kaufer, A., Stahl, O., Tubbesing, S., et al. 1999, *The Messenger*, 95, 8
- Kempton, E. M.-R., Bean, J. L., Louie, D. R., et al. 2018, *ArXiv e-prints*, arXiv:1805.03671
- Kipping, D. M. 2013, *MNRAS*, 435, 2152
- Kovács, G., Bakos, G. Á., Hartman, J. D., et al. 2010, *ApJ*, 724, 866
- Kozai, Y. 1962, *AJ*, 67, 591
- Lendl, M., Triaud, A. H. M. J., Anderson, D. R., et al. 2014, *A&A*, 568, A81
- Li, G., & Winn, J. N. 2016, *ApJ*, 818, 5
- Li, J., Tenenbaum, P., Twicken, J. D., et al. 2019, *PASP*, 131, 024506
- Luger, R., Agol, E., Foreman-Mackey, D., et al. 2019, *AJ*, 157, 64
- Mayor, M., Pepe, F., Queloz, D., et al. 2003, *The Messenger*, 114, 20
- Méndez, A., & Rivera-Valentín, E. G. 2017, *ApJL*, 837, L1
- Miller, N., & Fortney, J. J. 2011, *ApJL*, 736, L29
- Pepper, J., Pogge, R. W., DePoy, D. L., et al. 2007, *PASP*, 119, 923
- Petrovich, C., & Tremaine, S. 2016, *ApJ*, 829, 132
- Pollacco, D. L., Skillen, I., Collier Cameron, A., et al. 2006, *PASP*, 118, 1407
- Queloz, D., Anderson, D. R., Collier Cameron, A., et al. 2010, *A&A*, 517, L1
- Ricker, G. R., Winn, J. N., Vanderspek, R., et al. 2015, *Journal of Astronomical Telescopes, Instruments, and Systems*, 1, 014003
- Rodriguez, J. E., Quinn, S. N., Huang, C. X., et al. 2019, *AJ*, 157, 191
- Salvatier, J., Wiecki, T. V., & Fonnesbeck, C. 2016, *PeerJ Computer Science*, 2, e55
- Siverd, R. J., Brown, T. M., Barnes, S., et al. 2018, in *Society of Photo-Optical Instrumentation Engineers (SPIE) Conference Series*, Vol. 10702, *Ground-based and Airborne Instrumentation for Astronomy VII*, 107026C
- Smith, J. C., Stumpe, M. C., Van Cleve, J. E., et al. 2012, *PASP*, 124, 1000
- Southworth, J. 2011, *MNRAS*, 417, 2166
- Stassun, K. G., & Torres, G. 2018, *ApJ*, 862, 61
- Stumpe, M. C., Smith, J. C., Catanzarite, J. H., et al. 2014, *PASP*, 126, 100
- Sullivan, P. W., Winn, J. N., Berta-Thompson, Z. K., et al. 2015, *ApJ*, 809, 77
- Talens, G. J. J., Albrecht, S., Spronck, J. F. P., et al. 2017, *A&A*, 606, A73
- Theano Development Team. 2016, *arXiv e-prints*, abs/1605.02688. <http://arxiv.org/abs/1605.02688>
- Tokovinin, A. 2018, *PASP*, 130, 035002
- Tokovinin, A., Fischer, D. A., Bonati, M., et al. 2013, *PASP*, 125, 1336
- Twicken, J. D., Catanzarite, J. H., Clarke, B. D., et al. 2018, *PASP*, 130, 064502
- Wang, S., Jones, M., Shporer, A., et al. 2019, *AJ*, 157, 51
- Welch, P. D. 1967, *IEEE Trans. Audio & Electroacoust.*, 15, 70
- Ziegler, C., Tokovinin, A., Briceno, C., et al. 2019, *arXiv e-prints*, arXiv:1908.10871

Table 2. Prior and posterior parameters of the global fit. Derived parameters which are deterministic functions of the parameters fitted for are presented in the bottom part of the table. For the priors, $N(\mu, \sigma^2)$ stands for a normal distribution with mean μ and variance σ^2 , $N(\mu, \sigma^2; l, u)$ is a bounded normal distribution with lower and upper limits given by l and u , respectively, and $U(a, b)$ stands for a uniform distribution between a and b .

| Parameter | Prior | Value |
|--|-----------------------------------|---------------------------------------|
| P (days) | $N(11.27, 0.7^2)$ | 11.23660 ± 0.00011 |
| T_0 (BJD) | $N(2458547.4743, 0.0012^2)$ | $2458547.47448_{-0.00029}^{+0.00028}$ |
| $\ln(M_P/M_\oplus)$ | $N(\ln(500), 0.3^2)$ | $5.973_{-0.056}^{+0.054}$ |
| R_\star (R_\odot) | $N(1.282, 0.03^2)$ | $1.28_{-0.03}^{+0.03}$ |
| M_\star (M_\odot) | $N(1.17, 0.06^2)$ | 1.181 ± 0.058 |
| $r1^a$ | $U(0, 1)$ | $0.0942_{-0.0012}^{+0.0010}$ |
| $r2^a$ | $U(0, 1)$ | $0.723_{-0.024}^{+0.018}$ |
| u_1^{TESS} | $U(0, 1)$ | $0.50_{-0.27}^{+0.19}$ |
| u_2^{TESS} | $U(0, 1)$ | $-0.06_{-0.23}^{+0.33}$ |
| e | $N_b(0.4, 0.1; 0, 1)$ | 0.435 ± 0.024 |
| ω (rad) | $U(-\pi, \pi)$ | $1.230_{-0.063}^{+0.063}$ |
| γ_{FEROS} (m s^{-1}) | $N(-40, 20^2)$ | $-42.8_{-8.6}^{+8.8}$ |
| γ_{Coralie} (m s^{-1}) | $N(-20, 20^2)$ | $-26.9_{-15.4}^{+14.7}$ |
| γ_{CHIRON} (m s^{-1}) | $N(-20, 20^2)$ | $-20.9_{-10.6}^{+10.7}$ |
| γ_{NRES} (m s^{-1}) | $N(-20, 20^2)$ | $-28.5_{-11.4}^{+11.4}$ |
| $\gamma_{\text{Minerva}_T3}$ (m s^{-1}) | $N(0, 20^2)$ | $4.2_{-10.2}^{+10.1}$ |
| $\gamma_{\text{Minerva}_T4}$ (m s^{-1}) | $N(-20, 20^2)$ | $-32.2_{-10.5}^{+10.6}$ |
| $\gamma_{\text{Minerva}_T5}$ (m s^{-1}) | $N(0, 20^2)$ | $20.9_{-12.9}^{+12.7}$ |
| η_{FEROS} (m s^{-1}) | $N_b(13, 5^2; 0, \infty)$ | $13.5_{-3.1}^{+3.3}$ |
| η_{Coralie} (m s^{-1}) | $N_b(22, 10^2; 0, \infty)$ | $45.1_{-11.4}^{+12.4}$ |
| η_{CHIRON} (m s^{-1}) | $N_b(45, 15^2; 0, \infty)$ | $21.7_{-7.6}^{+8.0}$ |
| η_{Minerva} (m s^{-1}) | $N_b(30, 12^2; 0, \infty)$ | $33.0_{-3.8}^{+4.5}$ |
| η_S | $N_b(0.001, 0.0003^2; 0, \infty)$ | $0.00114_{-0.00010}^{+0.00011}$ |
| a_0 (m s^{-1}) | $N(0, 20^2)$ | $-6.4_{-8.2}^{+8.1}$ |
| a_1 ($\text{m s}^{-1} \text{ d}^{-1}$) | $N(0.7, 0.5^2)$ | 1.58 ± 0.19 |
| b_0 | $N(0, 0.1^2)$ | $-0.00197_{-0.00032}^{+0.00033}$ |
| b_1 (d^{-1}) | $N(0, 0.01^2)$ | $0.0204_{-0.0040}^{+0.0039}$ |
| b | | $0.723_{-0.024}^{+0.018}$ |
| i (deg) | | $87.63_{-0.1}^{+0.11}$ |
| R_P/R_\star | | $0.0942_{-0.0012}^{+0.0010}$ |
| $R_P(R_J)$ | | 1.170 ± 0.03 |
| $M_P(M_J)$ | | $1.236_{-0.067}^{+0.069}$ |
| a (AU) | | $0.1038_{-0.0017}^{+0.0017}$ |
| $T_{\text{eq}}(\text{K})^b$ | | 1252 ± 21 |

^aThese parameters correspond to the parametrization presented in [Espinoza \(2018\)](#) for sampling physically possible combinations of b and $p = R_P/R_\star$. We used an upper and lower allowed value for p of $p_l = 0.075$ and $p_u = 0.125$, respectively.

^bTime-averaged equilibrium temperature computed according to equation 16 of [Méndez & Rivera-Valentín \(2017\)](#)

Table 4. Relative photometry for TOI-677.^a

| BJD | f | σ_f | Instrument |
|--------------|--------|------------|------------|
| (2,400,000+) | ppt | ppt | |
| 58547.001330 | -0.199 | 0.789 | TESS |
| 58547.002719 | 1.058 | 0.790 | TESS |
| 58547.004108 | 0.339 | 0.789 | TESS |
| 58547.005496 | -1.082 | 0.790 | TESS |
| 58547.006885 | 0.377 | 0.790 | TESS |
| 58547.008274 | 1.051 | 0.790 | TESS |
| 58547.009663 | 0.314 | 0.789 | TESS |
| 58547.011052 | 1.058 | 0.790 | TESS |
| 58547.012441 | -0.483 | 0.790 | TESS |
| 58547.013830 | 0.617 | 0.789 | TESS |
| 58547.015219 | -0.675 | 0.790 | TESS |
| 58547.016608 | -0.039 | 0.789 | TESS |
| 58547.017997 | 0.166 | 0.790 | TESS |
| 58547.019386 | 0.393 | 0.788 | TESS |
| 58547.020774 | -0.916 | 0.790 | TESS |
| 58547.022163 | -1.167 | 0.789 | TESS |
| 58547.023552 | 2.311 | 0.790 | TESS |
| 58547.024941 | 1.251 | 0.790 | TESS |
| 58547.026330 | 0.043 | 0.789 | TESS |
| 58547.027719 | -0.603 | 0.790 | TESS |

^a Table 4 is published in its entirety in machine readable format. A portion is shown here for guidance regarding its form and content.

APPENDIX

Table 5. Radial velocities and bisector spans for TOI-677.^a

| BJD | RV ^b | σ_{RV} | BIS | σ_{BIS} | Instrument |
|--------------|----------------------|----------------------|----------------------|----------------------|------------|
| (2,400,000+) | (m s ⁻¹) | (m s ⁻¹) | (m s ⁻¹) | (m s ⁻¹) | |
| 58615.051551 | -26.62 | 5.4 | ... | ... | Minerva_T3 |
| 58615.051551 | -70.76 | 5.3 | ... | ... | Minerva_T4 |
| 58615.072962 | -26.25 | 5.4 | ... | ... | Minerva_T3 |
| 58615.072962 | -12.28 | 5.3 | ... | ... | Minerva_T4 |
| 58616.005135 | -43.36 | 5.4 | ... | ... | Minerva_T3 |
| 58616.026546 | -81.33 | 5.4 | ... | ... | Minerva_T3 |
| 58616.047945 | -81.42 | 5.4 | ... | ... | Minerva_T3 |
| 58618.484021 | -107.13 | 12.0 | 34 | 9 | FEROS |

Table 5 continued

Table 5 (*continued*)

| BJD (2,400,000+) | RV ^b (m s ⁻¹) | σ_{RV} (m s ⁻¹) | BIS (m s ⁻¹) | σ_{BIS} (m s ⁻¹) | Instrument |
|---------------------|---|---------------------------------------|-----------------------------|--|------------|
| 58619.499881 | -78.23 | 9.6 | 47 | 8 | FEROS |
| 58620.482581 | -54.73 | 11.3 | 14 | 9 | FEROS |
| 58621.616231 | 42.13 | 23.5 | -51 | 20 | Coralie |
| 58621.623201 | -14.62 | 13.3 | ... | ... | CHIRON |
| 58621.628071 | -20.13 | 13.3 | 23 | 10 | FEROS |
| 58621.948677 | -47.48 | 5.2 | ... | ... | Minerva_T4 |
| 58621.948677 | 67.59 | 5.4 | ... | ... | Minerva_T3 |
| 58621.970088 | -6.47 | 5.4 | ... | ... | Minerva_T4 |
| 58621.970088 | -27.69 | 5.4 | ... | ... | Minerva_T3 |
| 58622.467171 | -1.33 | 9.8 | 35 | 8 | FEROS |
| 58622.623371 | 14.93 | 23.1 | 86 | 20 | Coralie |
| 58622.626601 | 116.18 | 24.5 | ... | ... | CHIRON |

^a Table 5 is published in its entirety in machine readable format. A portion is shown here for guidance regarding its form and content.

^b For convenience, the mean has been subtracted from the originally measured radial velocities for each instrument, and the instrument-dependent radial velocity zeropoints reported in Table 2 are with respect to these mean-subtracted values. The mean values m which should be added to recover the original measurements are $m_{\text{FEROS}} = 37656.23$, $m_{\text{Coralie}} = 37665.27$, $m_{\text{CHIRON}} = 20.1$, $m_{\text{NRES}} = 38228.49$ and $m_{\text{Minerva}} = 37844.01$